Hydrodynamics, normal stress differences and heat transfer in rarefied pressure driven Poiseuille flow

2 authors:

Shashank Ravichandir
Leibniz Institute of Polymer Research Dresden
3 PUBLICATIONS **2** CITATIONS

Meheboob Alam
Jawaharlal Nehru Centre for Advanced Scientific Research
88 PUBLICATIONS **1,737** CITATIONS

Hydrodynamics, normal stress differences and heat transfer in rarefied pressure driven Poiseuille flow FREE

Shashank Ravichandir ✉; Meheboob Alam

Check for updates

View Online   Export Citation   CrossMark

AIP Publishing

Hydrodynamics, Normal Stress Differences and Heat Transfer in Rarefied Pressure Driven Poiseuille Flow

Shashank Ravichandir[a)] and Meheboob Alam

Engineering Mechanics Unit, Jawaharlal Nehru Centre for Advanced Scientific Research, Bengaluru, 560064, India

[a)]*Corresponding author: shashankravichandir@gmail.com*

Abstract. A parallelized Direct Simulation Monte Carlo (DSMC) solver is developed to solve the Boltzmann equation for the pressure-driven Poiseuille flow of monatomic gases over a range of Knudsen numbers in the slip and transitional regimes. The non-Newtonian and non-Fourier effects, along with hydrodynamic fields and rheology, are investigated and compared to the more widely studied acceleration-driven Poiseuille flow. The slip velocity is extracted from the velocity profiles and is expressed in terms of the Knudsen number as a power law. The non-Newtonian effects on stresses are characterised by defining two normal-stress differences whose variations in the stream-wise and wall-normal directions are studied. In addition, the normal and tangential heat fluxes are calculated from the simulation. To isolate the entrance and exit effects, the simulation is carried out for different aspect ratios of the channel keeping the pressure gradient constant. Finally this study is extended to the pressure-driven flow of rarefied granular gases.

INTRODUCTION

The flow driven by a constant body force or a pressure gradient for a fluid confined between two walls is known as the Poiseuille flow which has been of great interest to many researchers for over more than a century [1, 2, 3, 4, 5, 6]. The hydrodynamic fields as well as the rheology of the acceleration driven Poiseuille flows accounting for both, the departure from continuum hypothesis (characterized by the Knudsen number, the ratio of the mean free path to the characteristic length of the flow) and the effect of inelasticity (governed by the coefficient of restitution) of inter-particle collisions, have been studied extensively using the Direct Simulation Monte Carlo (DSMC) method [7] in the past few years [8, 9, 10, 11, 12]. Some of these effects include a bimodal shape of the temperature profile [4, 8, 12], non uniform pressure profiles and an anomalous parallel heat flux [9].

The challenges of extending the acceleration driven Poiseuille flow to a pressure driven Poiseuille flow are multi-fold. First, the implementation of constant pressure inlet and outlet boundary conditions at the particle level which is more difficult compared to the simpler boundary conditions that the acceleration driven case employs. Secondly, the hydrodynamic fields in the pressure driven case vary in both the longitudinal (stream-wise) and transverse (cross-stream) directions, whereas in the acceleration driven case quantities were invariant in the longitudinal direction. This leads to increased computing power owing to now having collision cells and averaging cells in two directions.

The first challenge has been resolved by a new two-step algorithm which allows us to implement constant pressure conditions and obtain smooth profiles of hydrodynamic fields. To tackle the second challenge, we have parallelized the code using Message Passing Interface (MPI) and have run the simulations on the ParamYukthi supercomputing cluster at JNCASR.

The remainder of the paper is divided as follows. We begin by describing the DSMC methodology, the implementation of boundary conditions, averaging procedure and introduce the control parameters. The hydrodynamics and rheology of molecular gases and their variations with Knudsen number are discussed in detail. We then discuss the effect of aspect ratio on the flows followed by a brief description of pressure-driven granular flow. We conclude the paper by summarizing the present results and discussing future work.

NUMERICAL METHOD

Direct Simulation Monte Carlo

The DSMC method is a particle based stochastic algorithm that solves the Boltzmann equation with fewer computational particles than the physical or real particles [13, 14]. Initially, N computational particles are distributed randomly in the simulation domain which is divided into cells for processing collisions and averaging. The algorithm consists

of two stages for every time step - streaming and collisions. In the streaming stage, the position vector and velocity vector of each particle is updated as

$$\overrightarrow{x}_i = \overrightarrow{x}_i + \overrightarrow{v}_i \Delta t + \frac{1}{2} \overrightarrow{a} \Delta t^2, \tag{1}$$

$$\overrightarrow{v}_i = \overrightarrow{v}_i + \overrightarrow{a} \Delta t, \tag{2}$$

where $\overrightarrow{a}$ is the external acceleration (for the pressure driven Poiseuille flow, we have $\overrightarrow{a} = 0$). Note that this updating is done only for the particles which are unaffected by the boundary conditions. Once the particles are advected and boundary conditions are applied (see next subsection), they are sorted out into their respective collision cells based on their positions.

For the collision stage, the number of collisions in a given time step in a cell of volume V_c is taken as [13]

$$N_c = \frac{2\pi R^2 N'^2 \langle |\overrightarrow{v}_{12}| \rangle \Delta t N_e}{V_c}, \tag{3}$$

where N' is the number of simulated particles in the cell, N_e is the ratio of real particles to simulated particles and $\overrightarrow{v}_{12} = \overrightarrow{v}_1 - \overrightarrow{v}_2$ is the relative velocity between two particles. The DSMC method processes this number of collisions (eqn. (3)) by randomly choosing N_p pairs of particles where

$$N_p = \frac{8\pi R^2 N'^2 v_{12}^{max} \Delta t N_e}{V_c}, \tag{4}$$

and selecting only certain pairs based on an acceptance-rejection scheme such that the number of pairs chosen is equal to N_c. A collision between two particles is accepted if,

$$\Theta(\overrightarrow{k} \cdot \overrightarrow{v_{12}}) |\overrightarrow{k} \cdot \overrightarrow{v}_{12}| > rand[0,1) v_{12}^{max}, \tag{5}$$

where Θ is the collision operator and $\overrightarrow{k}$ is an equidistributed random vector. The maximum relative velocity v_{12}^{max} is initially set to be thrice the mean probable velocity [10] and is dynamically updated to be the relative velocity of a chosen pair that exceeds the defined maximum relative velocity. Once a pair of particles have been accepted, the post collision velocities are calculated as:

$$\overrightarrow{v}_i = \overrightarrow{v}_i - \frac{1+e_n}{2} [(\overrightarrow{v}_i - \overrightarrow{v}_j) \cdot \overrightarrow{k}_{ij}] \overrightarrow{k}_{ij}, \tag{6}$$

$$\overrightarrow{v}_j = \overrightarrow{v}_j + \frac{1+e_n}{2} [(\overrightarrow{v}_i - \overrightarrow{v}_j) \cdot \overrightarrow{k}_{ij}] \overrightarrow{k}_{ij}, \tag{7}$$

where e_n is the coefficient of restitution and $\overrightarrow{k}_{ij}$ is the unit vector along the line joining the centers of the colliding spheres and can be taken as the same vector $\overrightarrow{k}$ that was used in the acceptance rejection scheme.

Boundary Conditions

The schematic of the problem is shown in Fig. 1. The domain is filled with hard spheres of diameter d and mass m. The division of the domain into collision cells is done along both the x and y directions to capture the variations of hydrodynamic fields in both directions. The boundary conditions for the system are periodic boundary conditions along the z-direction, thermal walls at $y = \pm L_y/2$ and constant pressure at $x = \pm L_x/2$.

The thermal walls [13, 15] are maintained at a temperature T_w. The particles after collision with the thermal wall undergo a change in all three velocities. The $x-$ and $z-$ components of the velocity are taken from a Gaussian distribution with variance $\frac{k_B T_w}{m}$, while the wall normal velocity (y-component) is sampled from a biased Gaussian and its direction is reversed -

$$v_x^{t+\Delta t} = \sqrt{\frac{k_B T_w}{m}} v_G, \tag{8}$$

$$v_y^{t+\Delta t} = \sqrt{\frac{2k_B T_w}{m}} v_{BG}, \tag{9}$$

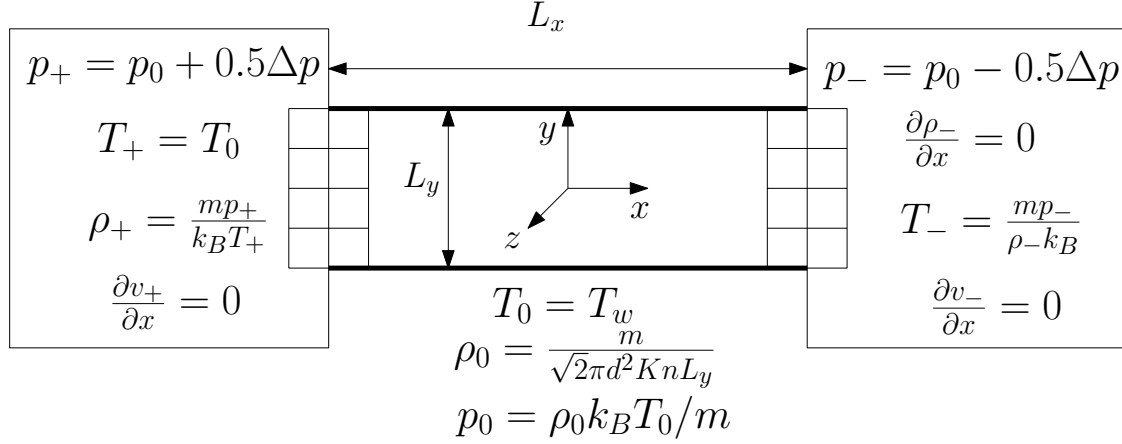$$v_z^{t+\Delta t} = \sqrt{\frac{k_B T_w}{m}} v_G. \tag{10}$$

$$p_+ = p_0 + 0.5\Delta p \qquad\qquad L_x \qquad\qquad p_- = p_0 - 0.5\Delta p$$

$$T_+ = T_0 \qquad\qquad\qquad \frac{\partial \rho_-}{\partial x} = 0$$

$$L_y \qquad\qquad y$$

$$\rho_+ = \frac{m p_+}{k_B T_+} \qquad\qquad x \qquad\qquad T_- = \frac{m p_-}{\rho_- k_B}$$

$$z$$

$$\frac{\partial v_+}{\partial x} = 0 \qquad\qquad T_0 = T_w \qquad\qquad \frac{\partial v_-}{\partial x} = 0$$

$$\rho_0 = \frac{m}{\sqrt{2}\pi d^2 K n L_y}$$

$$p_0 = \rho_0 k_B T_0 / m$$

FIGURE 1. Schematic of the pressure-driven Poiseuille flow in a channel of length L_x and width L_y bounded by two isothermal walls at $T = T_w$. The flow is driven by the pressure difference Δp along the x-direction.

Here v_G is a random number sampled from a Gaussian with zero mean and unit variance and v_{BG} is sampled from a biased Gaussian distribution -

$$p(v_{BG}) = \frac{m|v_{BG}|}{k_B T_w} exp\left(-\frac{m v_{BG}^2}{2 k_B T_w}\right). \tag{11}$$

The displacement of a particle ($\Delta \vec{x}$) affected by the wall boundary conditions over one time step is given by -

$$\Delta \vec{x} = \vec{v}^{\,t} t_{pre} + \vec{v}^{\,t+\Delta t} t_{post}, \tag{12}$$

where t_{pre} and t_{post} are the times within the timestep before and after the collision with the thermal wall.

To implement the constant pressure boundary condition [16] we add a layer of ghost cells on either side of the simulation domain along the x-direction to act as infinite reservoirs (see figure 1). After the streaming stage in every time-step the particles in these ghost cells are deleted and N_{req} number of particles, calculated from $\rho_\pm$ (see Fig. 1), are generated uniformly in the cells and their velocities are sampled from a Gaussian with mean equal to the average velocities in their adjacent cells in the x-directions and a standard distribution of $\sqrt{\frac{k_B T_\pm}{m}}$. This ensures that the inlet and outlet of the system are maintained at the required states as shown in Fig. 1.

In order to reduce the noise in the inlet and outlet velocities, we follow the following two step procedure. First, we run the code with $N = O(10^5)$ for a shorter period of time with the average velocities in the adjacent cells taken to be the running average of the past 50 time-steps. This is done to obtain the steady state inlet and outlet velocities as velocity is a first order moment and converges faster and with lesser number of particles. Then the code is run again with $N = O(10^6)$ with the inlet and outlet velocities, which are used as the mean for the Gaussian from which the generated particles are sampled, kept constant and are taken from step 1.

The code is parallelized by dividing the domain into a number of sub-domains, which is equal to the number of processing cores the code is intended to run on. The streaming (including the implementation of the boundary conditions) and collision of particles in different sub-domains are carried out simultaneously, and the information of the particles that leave or enter the sub-domain is communicated amongst the cores using message passing interface (MPI). The results obtained using this two step procedure (Fig. 2) were validated against the ones presented in Ref. [16] with excellent agreement with the current DSMC simulations producing smoother profiles.

Averaging Procedure

The averaging of the hydrodynamic fields is done over multiple snapshots of the system once the system has reached a steady state. The steady state is determined by observing the constancy of the total energy of all particles in the
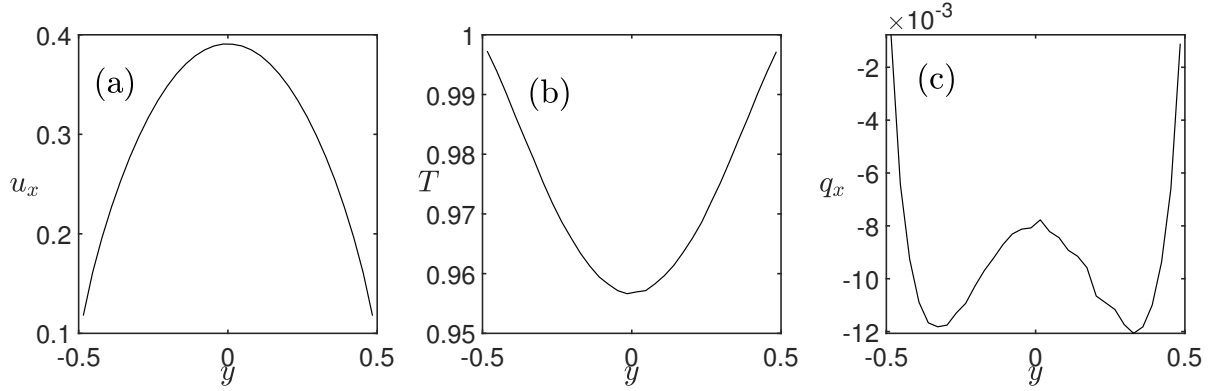
FIGURE 2. Transverse profiles of (a) streamwise velocity u_x, (b) temperature T, and (c) tangential heat flux q_x of a molecular gas undergoing pressure-driven Poiseuille flow at the middle of the channel $(x = 0)$: $\text{Kn} = 0.1$, $\Delta p = p_0$, and $L_x/L_y = 3$.

system [17, 18]. Given a particle level quantity $\psi(v)$, its macroscopic average in a given cell is given by

$$\langle \psi(\mathbf{v}) \rangle_{x,y,z} = \frac{1}{N_t} \sum_{t}^{N_t} \frac{1}{V_c} \sum_{i \in cell} \psi(\mathbf{v}_i(t)), \tag{13}$$

where $V_c = \delta_x \delta_y \delta_z$ is the volume of the cell and δ_x, δ_y and δ_z are the dimensions of the cell along the $x-$, $y-$ and $z-$ directions, respectively and N_t is the number of snapshots over which the quantity is averaged. Since the flow is invariant in the z-direction we obtain 2D fields of the macroscopic quantities by considering a single cell ($\delta_z = L_z$) in the z-direction. By choosing appropriate $\psi(v)$ we obtain the macroscopic/hydrodynamic fields such as velocity, temperature and density [8, 9] -

$$\rho(x,y) = \langle m \rangle_{x,y}, \tag{14}$$

$$\mathbf{u}(x,y) = \frac{1}{\rho(x,y)} \langle m\mathbf{v} \rangle_{x,y}, \tag{15}$$

$$T(x,y) = \frac{m}{3k_B\rho(x,y)} \langle (\mathbf{v} - \mathbf{u})^2 \rangle_{x,y}. \tag{16}$$

The stress tensor and heat flux vector are defined as :

$$\mathbf{P}(x,y) = \langle m(\mathbf{v} - \mathbf{u})(\mathbf{v} - \mathbf{u}) \rangle_{x,y}, \tag{17}$$

$$\mathbf{q}(x,y) = \frac{1}{2} \langle m(\mathbf{v} - \mathbf{u})^2 (\mathbf{v} - \mathbf{u}) \rangle_{x,y}. \tag{18}$$

The pressure is given by the trace of the stress tensor divided by the number of dimensions -

$$p = \frac{1}{3}(P_{xx} + P_{yy} + P_{zz}). \tag{19}$$

Control Parameters

The mass and the diameter of the particles of the gas are taken to be unity, the Boltzmann constant is taken as $k_B = 0.5$, the wall temperature, $T_w = T_0 = 1$ and the pressure difference is $\Delta p = p_0$. The width of the channel is fixed as $L_y = 1860d$ and the aspect ratio L_x/L_y is primarily set to 3 [16]. The calculation of p_0, ρ_0 and other inlet and outlet quantities are done using the relations listed in Fig. 1. The main control parameter is the Knudsen number -

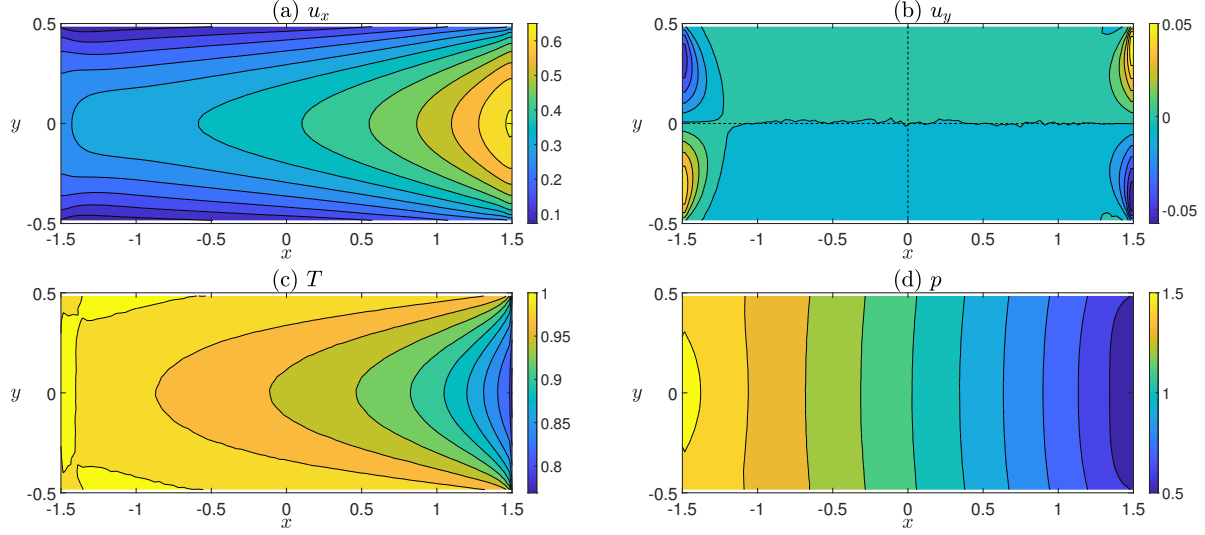$$\text{Kn} = \frac{\lambda}{\text{L}_y} = \frac{m}{\sqrt{2}\pi \text{d}^2 \rho_0 \text{L}_y}, \tag{20}$$

FIGURE 3. Contour plots of the hydrodynamic fields for $Kn = 0.1$: (a) stream-wise velocity u_x, (b) cross-stream velocity u_y, (c) temperature T and (d) pressure p. Other parameters are as in Fig. 2.

which is varied in the range $0.05 \leq Kn \leq 5$ by keeping the reference length L_y constant and changing the mean free path λ by changing the reference density ρ_0. When studying the effect of the aspect ratio, the length of the channel is varied keeping the width constant to obtain different aspect ratios (AR), $3 \leq AR \leq 9$. The sections on hydrodynamics, rheology and effect of aspect ratio correspond to molecular flows $(e_n = 1)$. When studying granular flows, the coefficient of restitution e_n is varied between 0.9 and 1.0.

The results of the pressure-driven flow are compared to those of the acceleration-driven flow presented in Refs. [10, 11], corresponding to the dimensionless acceleration of $\hat{a} = \frac{aL_y}{2k_BT_w/m} = 0.5$. It has been ensured that the forcing terms in the two cases, $dp/dx \approx \Delta p/L_x$ and $\rho_0 a$ are of comparable magnitudes for all Kn. For example, at $Kn = 0.1$, we have $dp/dx \approx 1.08 \times 10^{-7}$ and $\rho_0 a = 6.5 \times 10^{-7}$. By calculating the Mach and Reynolds numbers, the flows are found to be subsonic and laminar for all Kn.

In the remaining paper the density is normalized by ρ_0, temperature by T_0, pressure and stresses by p_0, velocity by $u_0 = \sqrt{2k_BT_0} = 1$ and heat fluxes by $\frac{1}{2}\rho_0 u_0^3$. The lengths are rescaled by L_y such that their range is $-1.5 \leq x \leq 1.5$ and $-0.5 \leq y \leq 0.5$.

HYDRODYNAMICS

The contour plots of the stream-wise velocity u_x, cross-stream velocity u_y, temperature T and pressure p for $Kn = 0.1$ are presented in Fig. 3 (contours of the density ρ look similar to the pressure contours and hence they are not shown). We observe that there is significant variation in both directions and the variation is of a greater magnitude in the stream-wise direction. To study these variation in more detail we consider two cross-sections along the center lines $(x = 0$ and $y = 0)$ as indicated by the dotted lines in Fig. 3(a). The variations of the hydrodynamic fields along these directions are shown in Fig. 4.

In Fig. 4(a) we see that the inlet and outlet pressures are indeed $1.5p_0$ and $0.5p_0$, respectively, irrespective of the Kn. We see that the pressure variation is linear in first order and is not highly dependent on Kn. The temperature of the gas decreases sharply along the length of the channel (Fig. 4(b)) and at any point the temperature increases with increasing Kn. From the pressure and temperature profiles dependence on Kn and the equation of state $(p = \rho k_B T/m)$ we can deduce that the density, which decreases along the channel, decreases with increase in Kn (Fig. 4(c)). The stream-wise velocity u_x (Fig. 4(d)) increases along the length of the channel and decreases with increasing Kn. Ignoring inlet and outlet effects, we observe from Fig. 4(a-d) that all hydrodynamic quantities vary monotonically along the length of the channel.

Coming to the wall-normal variation of the hydrodynamic fields at $x = 0$ (Fig. 4(e-h)) we immediately observe that
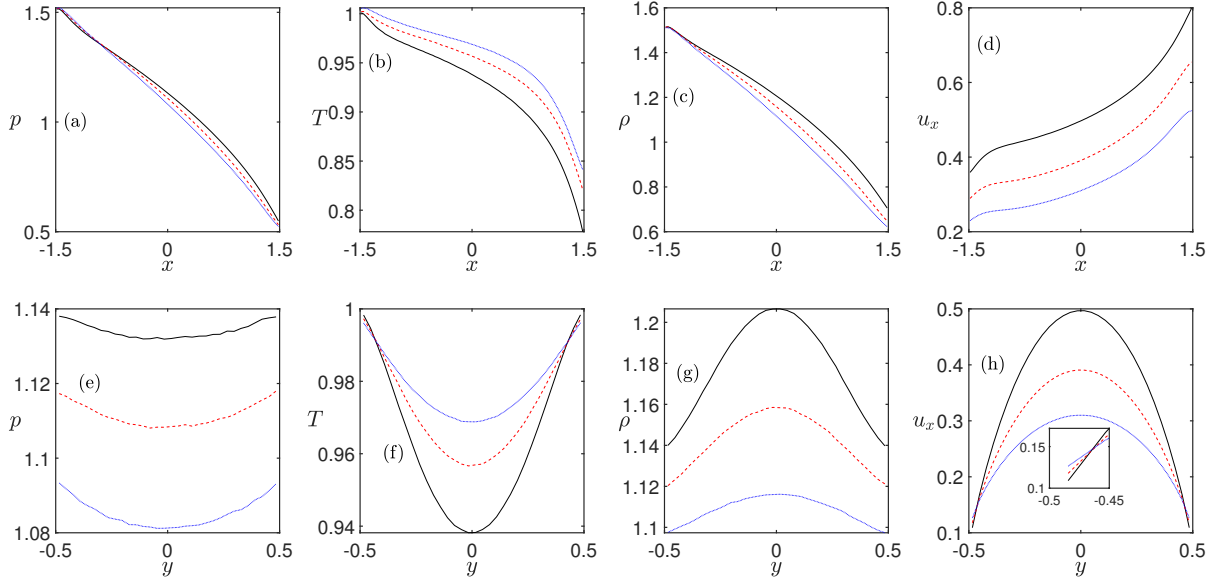
FIGURE 4. (a,b,c,d) Stream-wise variations of hydrodynamic fields along $y = 0$ line and (e,f,g,h) their cross-stream variations along $x = 0$ line. Solid line : Kn = 0.05, Dashed line : Kn = 0.1 and Dotted line : Kn = 0.2.

their variations are an order of magnitude lower compared to their stream-wise variation. The variations of pressure (Fig. 4(e)) and velocity (Fig. 4(h)) are similar to those of the acceleration-driven flow [8]. The first difference we encounter is in the temperature profiles where instead of the well-known bimodal structure [4, 8, 10] we have convex upwards profiles with the degree of convexity decreasing with increasing Kn. Similarly for the density field we have concave downward profiles instead of the convex upward profiles observed in acceleration driven flows.

Slip Velocity

The first rarefied gas effect we characterize is the slip velocity at the walls defined as -

$$u_s(x) = \frac{1}{2}(u_x(x, 0.5) + u_x(x, -0.5)). \tag{21}$$

The variation of u_s along the length of the channel is shown in Fig. 5(a). Ignoring entrance and exit effects, we see that the slip velocity increases in the stream-wise direction and as expected increases with increase in Knudsen number. The variation of the slip velocity at the center of the channel $u_s(x = 0)$ with the Knudsen number is shown in Fig. 5(b). We can see that u_s vs *Kn* profile is qualitatively different compared to that of the acceleration driven flow shown in the inset (our simulation data for acceleration driven flow was validated with the data presented in Ref. [10]). To ascertain the dependence of slip velocity on Knudsen number we first compare it to the Maxwell-Navier slip boundary condition [18, 19] -

$$u_s \propto \frac{\mathrm{Kn}}{\rho_w} \frac{du}{dy}\bigg|_w = \mathrm{Kn_w u'_w}, \tag{22}$$

where ρ_w is the gas density at the walls, $\mathrm{Kn_w} = \mathrm{Kn}/\rho_w$, and $u'_w = \frac{du}{dy}\big|_w$. The variation of the velocity gradient at the walls u'_w is plotted in Fig. 5(c). To check the validity of the Maxwell-Navier slip boundary condition we define a velocity slip length $\zeta = u_s/u'_w$ and plot its variation with Kn_w in Fig. 5(d). We see that the profile is linear only for small values of Kn_w. Therefore we come up with a modified Maxwell-Navier slip boundary condition -

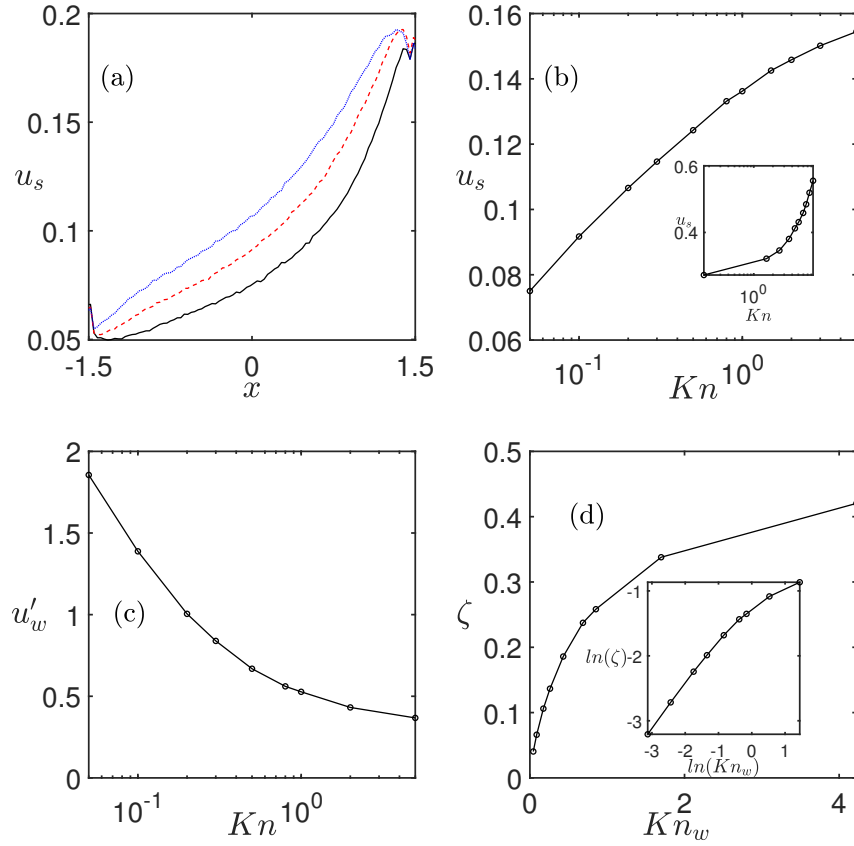$$u_s \propto \mathrm{Kn_w^\delta u'_w} + \mathrm{h.o.t}, \tag{23}$$

FIGURE 5. (a) Variations of the slip velocities along the length of the channel. [Solid line: Kn = 0.05, Dashed line : Kn = 0.1 and Dotted line : Kn = 0.2]. (b) Variation of the slip velocity at channel centre with Knudsen number (Inset - same for acceleration driven flow). (c) Variation of the gradient of velocity at the walls at $x = 0$ with Knudsen number. (d) Variation of $\zeta = u_s/u'_w$ with $Kn_w = Kn/\rho_w$ (Inset - logarithm of both quantities).

where δ is nearly constant ($\delta \approx 0.712$) for Kn ≤ 1 and decreases slightly with increasing Kn for Kn > 1 (see inset of Fig. 5(d)). Note that Eq. (23) is a first order approximation that can be used to predict the slip velocities only at small values of Kn. Also note that the value of $\delta = 0.712$ has been calculated for $\Delta p = p_0$ at $x = 0$. The effects of pressure gradient and other hydrodynamic fields on slip velocity needs to be investigated in future.

RHEOLOGY

Normal Stress Differences

The diagonal components of the stress tensor defined by (17) are different from each other. Thus we define two normal stress differences [20, 21, 22, 23, 24] :

$$\mathcal{N}_1 = \frac{p_{xx} - p_{yy}}{p},\tag{24}$$

$$\mathcal{N}_2 = \frac{p_{yy} - p_{zz}}{p},\tag{25}$$

scaled by the mean pressure. The normal stress differences are a measure of the deviation of the flows from being Newtonian where $\mathcal{N}_1 = 0 = \mathcal{N}_2$ corresponds to Newtonian or non-rarefied flows [20]. From the streamwise variations
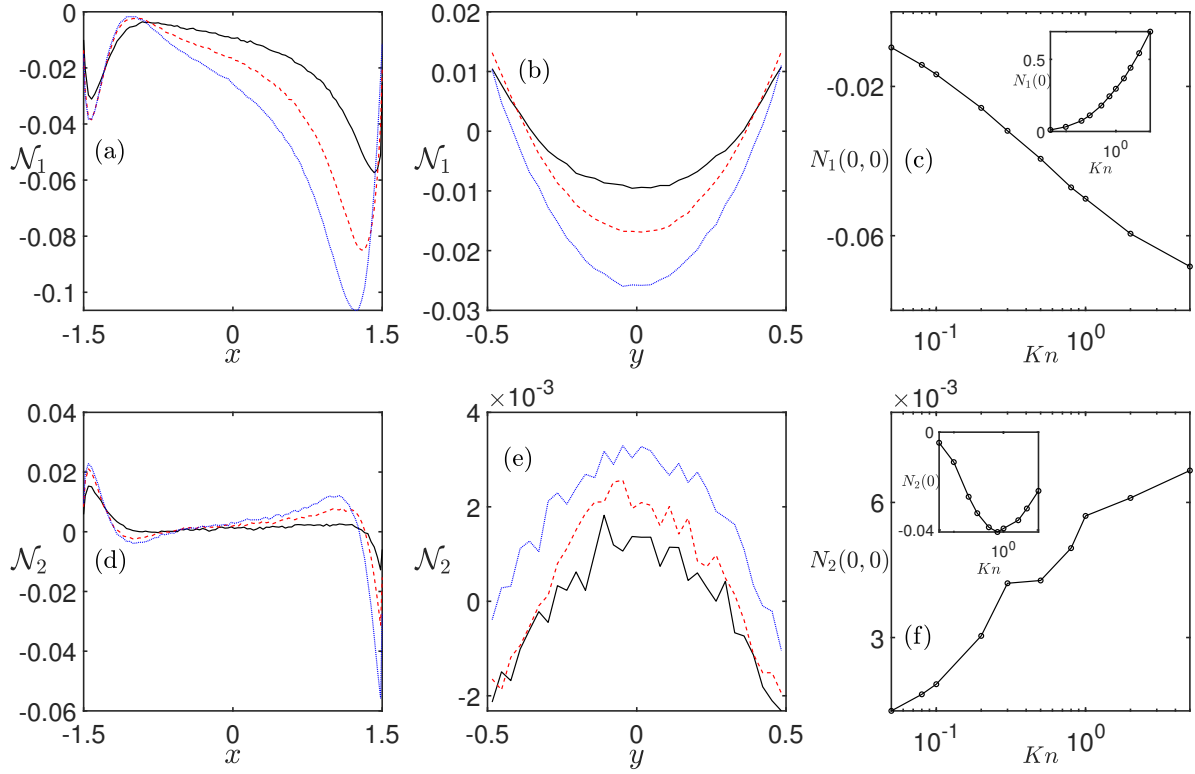
FIGURE 6. (a,d) Stream-wise variations along $y = 0$ and (b,e) cross-stream variations along $x = 0$ of $\mathcal{N}_1$ and $\mathcal{N}_2$ respectively [Solid line: Kn = 0.05, Dashed line : Kn = 0.1 and Dotted line : Kn = 0.2]. (c,f) Variations of $\mathcal{N}_1$ and $\mathcal{N}_2$ at (0,0) with Knudsen number (Insets display (c)$\mathcal{N}_1$ and (f)$\mathcal{N}_2$ for acceleration driven flow at $y = 0$).

of the two normal stress differences (Fig. 6(a),6(d)) we observe that the magnitudes of both $\mathcal{N}_1$ and $\mathcal{N}_2$ increase along the length of the channel monotonically neglecting the inlet and outlet effects. From the cross-stream variations (Fig. 6(b), 6(e)) we see that $\mathcal{N}_1$ is an order of magnitude higher compared to $\mathcal{N}_2$ and that the magnitudes of $\mathcal{N}_1$ and $\mathcal{N}_2$ at $x = 0$ are the highest at the channel centre ($y = 0$). Plotting $\mathcal{N}_1(0,0)$ and $\mathcal{N}_2(0,0)$ against the Knudsen number, we see that both quantities increase with increasing in Kn on account of increased rarefied effects. Comparing them with the corresponding plots of the acceleration-driven case (see insets of Fig. 6(c) and 6(f), where we validate our simulation results with the ones presented in Ref. [10]), we see that the normal stress differences are of opposite signs compared to their acceleration-driven counterparts and are of opposite signs to each other. The latter observation is consistent with the theoretical and numerical findings in the acceleration driven Poseuille flow [20, 21, 22, 23, 24].

Heat Fluxes

The cross-stream variations of the wall normal heat flux q_y and the tangential heat flux q_x at $x = 0$ are shown in Fig. 7(a) and 7(b), respectively. Comparing them to their acceleration-driven flow counterparts (see insets, where our simulation results were validated using the results in Ref. [11]), we observe that the direction of q_y is reversed and is from the walls to the channel center. This can be understood from the Fourier law of heat conduction -

$$\boldsymbol{q} = -\boldsymbol{\kappa} \nabla T, \tag{26}$$

where $\boldsymbol{\kappa}$ is the conductivity tensor, and the differences in the temperature profiles discussed before (Fig. 4(f)) causes the change in the sign of ∇T for two cases.

The tangential heat flux (q_x) in acceleration driven flow is due to non-zero diagonal terms of the conductivity tensor $\boldsymbol{\kappa}$ [9, 11], which arise due to rarefaction effects and the q_x profiles are single-welled in nature (see inset of Fig.
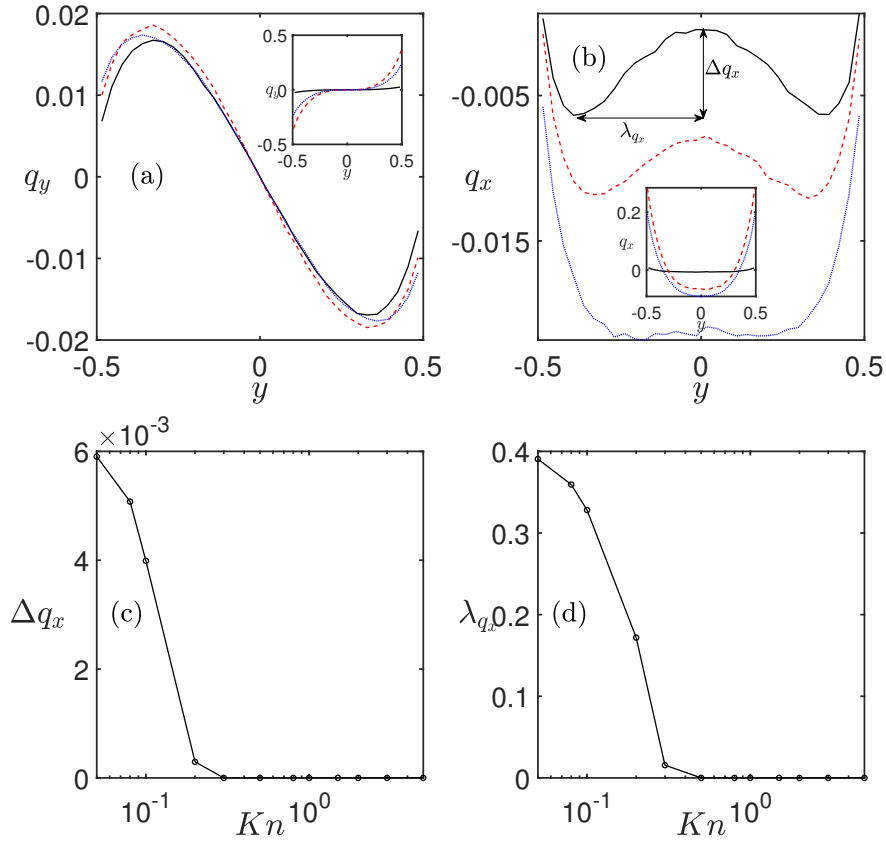
FIGURE 7. (a,b) Cross-stream variations of tangential flux and wall normal heat flux along $x = 0$ respectively (Insets - same for acceleration driven flow) [Solid line: Kn = 0.05, Dashed line : Kn = 0.1 and Dotted line : Kn = 0.2]. (c,d) The variation of Δ_{q_x} and λ_{q_x} against Knudsen number respectively.

7(b)). It was found that these q_x profiles develop a double-welled structure for granular flow due to the effects of inelasticity [11]. In the pressure-driven Poiseuille flow we have a temperature gradient in the stream-wise direction ($x-$direction) driving the tangential heat flux (26), and we observe a double-well structure in the q_x profiles (Fig. 7(b)) for molecular gases (no inelastic effects), which transitions into a single well structure with increasing Knudsen number. To quantitatively characterize this transition we introduce two parameters, (i) Δ_{q_x} a measure of the relative depth of the two wells with respect to the channel centre and (ii) λ_{q_x} the distance of the minima from the channel centre. Plotting these as a function of Knudsen number we see that both parameters go to zero as Kn $\gg 0.1$ thus confirming that the double-well structure is a continuum effect.

EFFECT OF ASPECT RATIO

So far the study had been done with a constant aspect ratio ($AR = L_x/L_y$) of 3. To study the effects of changing the aspect ratio on the flows we keep the width of the channel constant and change its length to obtain three different aspect ratios. To simulate similar flow scenarios we also keep the pressure gradient ($\Delta p/L_x$) constant. The simulations are run at Kn = 0.1 and $dP/dx \approx 3.24 \times 10^{-8}$ for all aspect ratios. The comparison for the three different aspect ratios is presented in Fig. 8 which shows the stream-wise variations of the hydrodynamic fields at $y = 0$. Note that the lengths have been rescaled with the respective L_x's such that $-0.5 \leq x \leq 0.5$ for all cases.

The first thing to note from Fig. 8 is that the entrance and exit lengths (the lengths from the entrance and exit at which the local maxima in the u_x profile occurs) decrease with increase in aspect ratio. Keeping the pressure gradient constant and changing the length gives rise to different inlet and outlet pressures as can be seen in Fig. 8(a). The
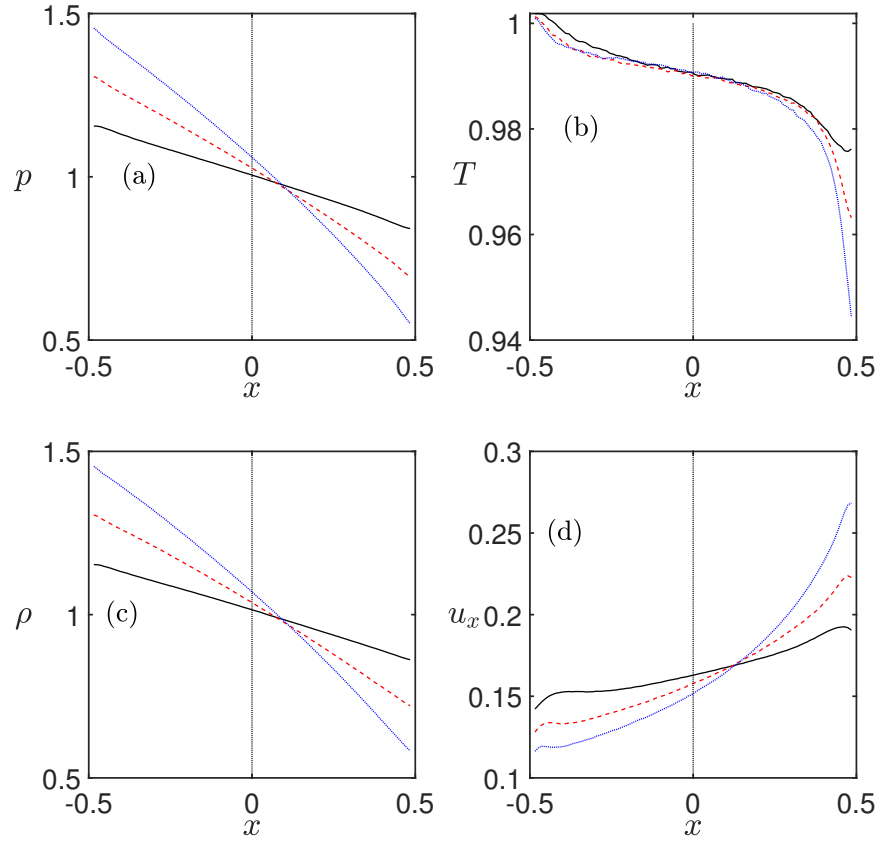
FIGURE 8. Streamwise variations of hydrodynamic fields along $y = 0$ for different aspect ratios. Solid line : Aspect Ratio = 3, Dashed line : Aspect Ratio = 6 and Dotted line : Aspect Ratio = 9.

temperature variation is nearly identical in the bulk of the channel (Fig. 8(b)). From the pressure and temperature profiles we can deduce the density profiles (Fig. 8(c)) which closely follow the pressure profiles. We also observe that the stream-wise velocity profiles differ by changing the aspect ratio (Fig. 8(d)). However at the centre of the channel ($x = 0$), we see that the profiles are converging, and our analysis of slip velocity, normal stress differences and heat fluxes so far can be assumed to remain valid irrespective of the aspect ratio.

GRANULAR FLOWS

A granular gas is defined as a system of randomly moving particles interacting via inelastic collisions [25, 26, 27, 28, 29]. By changing the coefficient of restitution in (6) and (7) we can simulate the pressure-driven Poiseuille flow of rarefied granular gases. Here we have carried out a preliminary study for four different coefficients of restitution - $e_n = 1, 0.99, 0.95, 0.9$ at Kn = 0.1, Aspect Ratio = 3, and $\Delta p / p_0 = 1$. The contour plots of the hydrodynamic fields for $e_n = 0.95$ are shown in Fig. 9. There are noticeable differences in these contour plots compared to those of molecular gases(Fig. 3). To study the effect of e_n, we plot the stream-wise and cross-stream variations in Fig. 10. We observe two interesting effects due to the addition of inelasticity: (i) there is a non-monotonic variation of hydrodynamic fields (see pressure, density and velocity u_x plots) along the stream-wise direction; (ii) there is a clustering effect [29] due to which a large increase in density is found near the exit of the channel for lower coefficients of restitution. Both effects need to be further investigated.
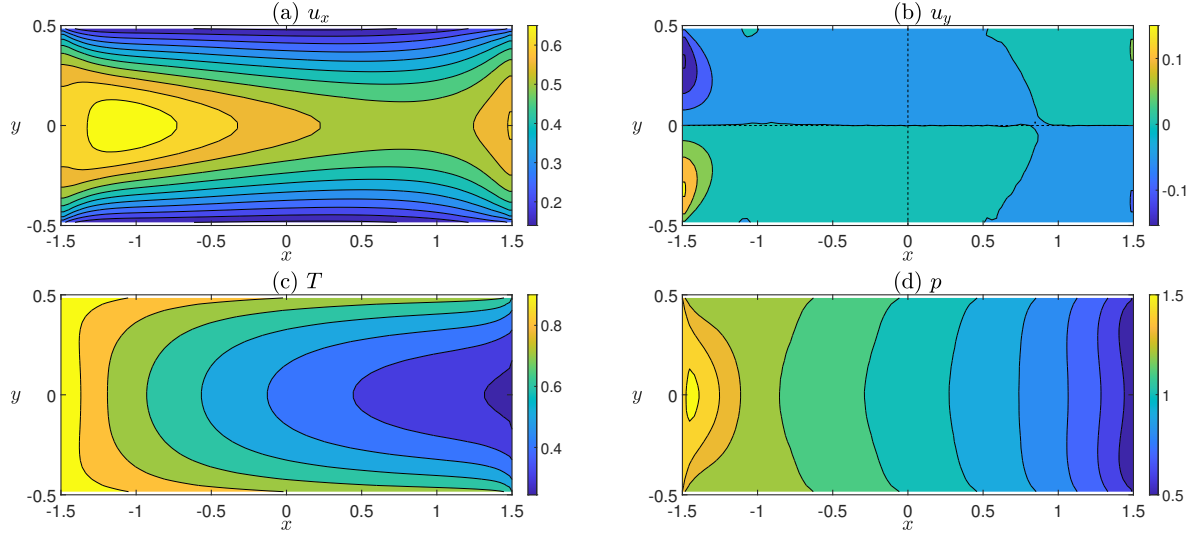
FIGURE 9. Contour plots of the hydrodynamic fields for Kn = 0.1 and $e_n = 0.95$: (a) stream-wise velocity u_x, (b) cross-stream velocity u_y, (c) temperature T and (d) pressure p .
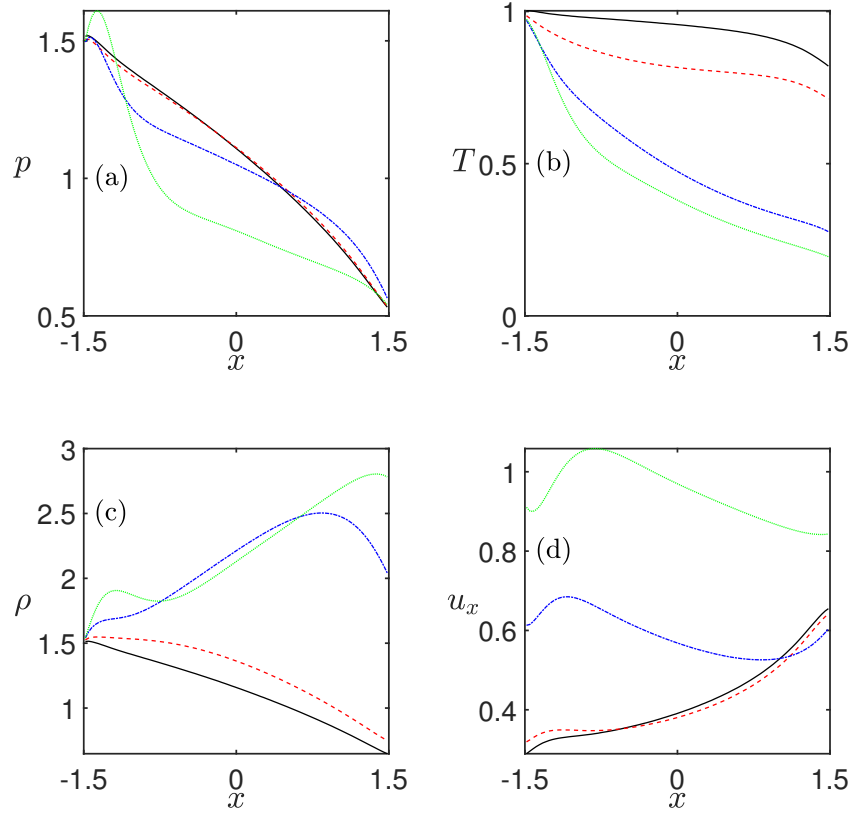
FIGURE 10. Stream-wise variations of hydrodynamic fields along $y = 0$ for granular Poiseuille flow with coefficients of restitution e_n. Solid line : $e_n = 1.0$, Dashed line : $e_n = 0.99$, Dashed-dotted line : $e_n = 0.95$ and Dotted line : $e_n = 0.9$.

CONCLUSION

We implemented a two-step DSMC algorithm that yields smooth hydrodynamic profiles in a comparatively lesser time than with the existing implementation of pressure boundary conditions [16]. We studied the variations of these profiles with the Knudsen number (Kn) and compared them to the acceleration-driven Poiseuille flow. From the velocity data, we extracted the slip velocity and found a modified Maxwell-Navier slip boundary condition. To quantify the rarefaction driven non-Newtonian effects we defined two normal stress differences and studied their variations with Kn. We studied the heat flux profiles and characterized the transition from continuum flow to rarefied flow via the transition from the double-welled to single-welled structure of the tangential heat flux profile. The effect of the aspect ratio of the channel on the hydrodynamic fields has been analyzed. Finally we carried out a preliminary study of pressure driven granular flow.

A quantitative study on the effects of aspect ratio and pressure gradient on the entrance and exit lengths and a detailed study of the granular pressure-driven Poiseuile flow on a 2D $Kn - e_n$ parameter space are left for a future work. Extending this work to a dense gas could also be considered in a future work.

ACKNOWLEDGMENTS

REFERENCES

1. M. Knudsen, *Annalen der Physik* **333**, 75–130 (1909).
2. C. Cercignani and A. Daneri, *J. Appl. Phys.* **34**, 3509–3513 (1963).
3. T. Ohwada, Y. Sone, and K. Aoki, *Phys. Fluids A* **1**, 2042–2049 (1989).
4. M. Tij and A. Santos, *J. Stat. Phys.* **76**, 1399–1414 (1994).
5. K. Aoki, S. Takata, and T. Nakanishi, *Phys. Rev. E* **65**, 026315 (2002).
6. N. G. Hadjiconstantinou, *J. Heat Trans.* **125**, 944–947 (2003).
7. G. Bird, *Phys. Fluids* **13**, 2676–2681 (1970).
8. M. M. Mansour, F. Baras, and A. L. Garcia, *Phys. A* **240**, 255–267 (1997).
9. F. Uribe and A. L. Garcia, *Phys. Rev. E* **60**, 4063 (1999).
10. R. Gupta and M. Alam, *Phys. Rev. E* **95**, 022903 (2017).
11. M. Alam, R. Gupta, and S. Ravichandir, *Phys. Rev. Fluids* **6**, 114303 (2021).
12. M. Tij and A. Santos, *J. Stat. Phys.* **117**, 901–928 (2004).
13. G. Bird, *Molecular Gas Dynamics and the Direct Simulation of Gas Flows* (Clarendon Press, 1994).
14. T. Pöschel and T. Schwager, *Computational Granular Dynamics: Models and Algorithms* (Springer Science & Business Media, 2005).
15. C. Cercignani, *Rarefied Gas Dynamics: From Basic Concepts to Actual Calculations*, Vol. 21 (Cambridge University Press, 2000).
16. Y. Zheng, A. L. Garcia, and B. J. Alder, *J. Statist. Phys.* **109**, 495–505 (2002).
17. M. Alam, A. Mahajan, and D. Shivanna, *J. Fluid Mech.* **782**, 99–126 (2015).
18. V. Chikkadi and M. Alam, *Phys. Rev. E* **80**, 021303 (2009).
19. J. C. Maxwell, *Phil. Trans. R. Soc. London* , 231–256 (1879).
20. N. Sela and I. Goldhirsch, *J. Fluid Mech.* **361**, 41–74 (1998).
21. S. Saha and M. Alam, *J. Fluid Mech.* **757**, 251–296 (2014).
22. S. Saha and M. Alam, *J. Fluid Mech.* **795**, 549–580 (2016).
23. M. Alam and S. Luding, *Phys. Fluids* **15**, 2298–2312 (2003).
24. M. Alam and S. Luding, *Powders and Grains* (ed. R. Garcia-Rojo, HJ Herrmann & S. McNamara) , 1141–1144 (2005).
25. C. S. Campbell, *Ann. Rev. Fluid Mech.* **22**, 57–90 (1990).
26. J. T. Jenkins and M. Richman, *Phys. Fluids* **28**, 3485–3494 (1985).
27. J. Montanero, V. Garzó, A. Santos, and J. Brey, *J. Fluid Mech.* **389**, 391–411 (1999).
28. T. Pöschel and S. Luding, *Granular Gases*, Vol. 564 (Springer Science & Business Media, 2001).
29. I. Goldhirsch, *Ann. Rev. Fluid Mech.* **35**, 267 (2003).